12,05

Structure and properties of $Co_xMn_{1-x}Fe_2O_4$ nanoparticles depending on the amount of Co ions ($0 \leq x \leq 1.0$)

© A.S. Kamzin[1], I.M. Obaidat[2], V.G. Semenov[3], V. Narayanaswamy[4], I.A. Al-Omari[5], B. Issa[6], I.V. Buryanenko[7]

[1] Ioffe Institute,
St. Petersburg, Russia
[2] Department of Physics, United Arab Emirates University,
Al-Ain 15551, UAE
[3] St. Petersburg State University,
St. Petersburg, Russia
[4] Research Institute of Medical & Health Sciences, University of Sharjah,
Sharjah 27272, UAE
[5] Department of Physics, Sultan Qaboos University,
P.O. Box 36, Muscat PC 123, Sultanate of Oman
[6] Department of Medical Diagnostic Imaging, College of Health Sciences, University of Sharjah,
Sharjah, P.O. Box 27272, UAE
[7] Peter the Great Saint-Petersburg Polytechnic University,
St. Petersburg, Russia

E-mail: ASKam@mail.ioffe.ru

Received February 26, 2022
Revised February 26, 2022
Accepted March 10, 2022

The properties of magnetic nanoparticles (MNPs) of spinel ferrites $Co_xMn_{1-x}Fe_2O_4$ (at $x = 0.0$; 0.2; 0.3; 0.4; 0.5; 0.6; 0.8; 1.0) synthesized by chemical co-precipitation method have been studied. The studies of the synthesized $Co_xMn_{1-x}Fe_2O_4$ MNPs were carried out using X-ray diffraction (XRD), Raman scattering and Mössbauer spectroscopy. The results of XRD, Raman and Mössbaur studies indicate that the obtained $Co_xMn_{1-x}Fe_2O_4$ MNPs are single-phase. It was established from XRD measurements that the average size of $Co_xMn_{1-x}Fe_2O_4$ crystallites is 34.86 nm for $MnFe_2O_4$ ($x = 0$) and decreases to 14.99 nm for $CoFe_2O_4$ ($x = 1.0$) with increasing Co ions concentration. An analysis of the Mössbaur spectra showed that the average crystallite size varies from 25 nm for $MnFe_2O_4$ ($x = 0$) to 12 nm for $CoFe_2O_4$ ($x = 1.0$). On the Raman spectra of $Co_xMn_{1-x}Fe_2O_4$ MNPs, in the region of $\sim 620\,cm^{-1}$, splitting of the A1g line is observed, which means that the studied MNPs have a reverse spinel structure. The intensity ratio of the A1g (1) and A1g (2) peaks indicates a significant redistribution of the Co^{2+} and Fe^{3+} cations between tetra- and octahedralpositions in MNPs of the $Co_xMn_{1-x}Fe_2O_4$ ferrite, which is confirmed by Mössbauer data. Mössbaur spectroscopy data indicate that the synthesized $Co_xMn_{1-x}Fe_2O_4$ MNPs consist of large particles with magnetic ordering and small particles in the paramagnetic phase. With an increase in the concentration of Mn ions, the proportion of fine particles increases, which leads to a decrease in the magnetic blocking temperature. The saturation magnetization of MNPs at $x = 0.2$ ($Co_{0.2}Mn_{0.8}Fe_2O_4$) is 57.41 emu/g and this sample, as was found in [V. Narayanaswamy, I.A. Al-Omari, A.S. Kamzin, B. Issa, H.O. Tekin, H. Khourshid, H. Kumar, A. Mallya, S. Sambasivam, I.M. Obaidat. Nanomaterials **11**, 1231 (2021)] has the highest specific absorption rate. As shown by Mössbauer studies, this is due to the fact that these particles are in a superparamagnetic state and the magnetic blocking temperature of these MNPs is in the region of ~ 315 K, which is most suitable for the treatment of malignant tumors by magnetic hyperthermia. Thus, the synthesized $Co_xMn_{1-x}Fe_2O_4$ MNPs are promising for biomedical applications.

Keywords: spinel ferrites $Co_xMn_{1-x}Fe_2O_4$, magnetic structure, superparamagnetism, Mössbauer spectroscopy, materials for biomedicine.

DOI: 10.21883/PSS.2022.06.53838.298

1. Introduction

Substantial differences of properties of the magnetic nanoparticles (MNPs) from their bulk analogs and uniqueness of the MNP characteristics are of huge interest of researchers both in terms of fundamental studies of the magnetic nanoparticles [1–4] and practical applications (see, for example,the paper [5] and references therein), including usage in various biomedicine fields [6–10].

The most utilized in the biomedicine are magnetic nanoparticles of magnetite (Fe_3O_4), which is due to its biological compatibility. However, the biomedicine application of the magnetite is limited by its toxicity due to Fe^{2+} ions [6] as well as by weak magnetic characteristics.

The search for new magnetic particles with higher and more biocompatible characteristics, wherein advantages inherent to the iron oxide MNPs are not lost, has led the researchers to ferrites with a spinel structure with the general formula $M^{2+}Fe_2^{3+}O_4^{2-}$, where M^{2+} are two-valence ions of metals (Ni, Cu, Co, Mn, etc.) [4,8–11]. In comparison with the magnetite, these spinel ferrites (SF) have higher magnetic characteristics and better chemical resistance [10,11]. SF magnetism formation is sourced in superexchange interactions of cations in tetrahedral (A) and octahedral (B) positions via oxygen ions, these are the exchanges A−B as well as B−B and A−A (see, for example, [5,7]). Therefore, the magnetic properties of the spinel ferrite are correlated to the distribution of the cations by the A and B positions, by varieties of the cations, which is determined by the SF chemical composition. Extensive studies of SF MNPs have resulted in the fact that the chemical composition and synthesis methods significantly affect not only particle sizes and an SF structure, but electric, optic and magnetic SF properties, such as magnetization, anisotropy, coercive and hyperfine fields [6,8–11]. By technological methods and ion alloying of the metals, it is possible to control ion distribution across nonequivalent positions of the crystal lattice, a structure of a surface layer, a type of crystal faceting of particles, and therefore, to change and adapt their physical properties for various purposes and, consequently, to synthesize the SF MNPs with required specific properties [8–22]. For biological compatibility of the MNPs surfaces of the SF particles, such as $MnFe_2O_4$, $MgFe_2O_4$, $CoFe_2O_4$, $ZnFe_2O_4$, can be easily modified and/or properly functionalized without damaging their external magnetic field's controllability to produce good-quality materials to amplify contrast of magnetic resonance imaging images and treatment of malignant tumors by means of magnetic hyperthermia. The above-listed advantages of the SF MNPs, as well as their lower toxicity, lower values of saturation magnetization, high corrosion resistance, magnetocrystalline anisotropy and magnetic susceptibility, minor coercivity and high stability and colloidal dispersibility in saline liquids make the SF MNPs especially promising for biomedicine [8–21].

In their attention to spinel ferrites, the researchers are attracted by manganese ($MnFe_2O_4$) and cobalt ($CoFe_2O_4$) ferrites due to their chemical stability, catalytical activity, natural abundance, a high specific heat capacity, a low melt temperature, which can be adapted for various applications [4,8,9,17–24]. The $CoFe_2O_4$ ferrite — a well known magnetically hard material, which is used in various fields and in the biomedicine due to high levels of magnetocrystalline anisotropy, coercivity and magnetooptical coefficients, moderate saturation magnetization, good-quality chemical stability and mechanical hardness [20–24]. The $MnFe_2O_4$ SF MNPs (a magnetically soft material with low magnetocrystalline anisotropy) are of big interest due to the biocompatibility of the Mn^{2+} ions, controllable magnetic properties and excellent chemical stability [8,9,17–20,24]. The $MnFe_2O_4$ nanoparticles were reported in the paper [25] as being a new material for magnetic hyperthermia and MRI-contrast. The important advantage of the Mn-based ferrites is that manganese can be consumed by a human body in a quantity of 0.67−4.99 mg at the average demand of 2.21 mg per day [26].

But, the high magnetocrystalline anisotropy of the $CoFe_2O_4$ nanoparticles impedes obtaining a high initial susceptibility required for biomedicine applications. On the other hand, the low magnetocrystalline anisotropy of the $MnFe_2O_4$ SF MNPs provides for an effective way of reducing the anisotropy of the $CoFe_2O_4$ particles by creating the $Co_xMn_{1-x}Fe_2O_4$ solid solution, in which a part of the Co^{2+} ions is substituted by the Mn^{2+} ions. As a result, it was established that it is possible to control properties of the $Co_xMn_{1-x}Fe_2O_4$ solid solutions which combine the $MnFe_2O_4$ and $CoFe_2O_4$ spinels (which are so different in their characteristics) during their synthesis and to produce single-phase mixed solid solutions $Co_xMn_{1-x}Fe_2O_4$, which have unique magnetic properties and a wide range of the applications, including in the biomedicine (for example, MRI, medicine delivery, magnetic hyperthermia) [9,10,14,15,27–37].

Thus, it was established that the saturation magnetization of the $Co_xMn_{1-x}Fe_2O_4$ MNPs is maximum when $x = 0.3$, but reduces with further increase in the Mn concentrations [38]. The $MnxCo_{1-x}Fe_2O_4$ MNPs can decompose contaminants more effectively than pure cobalt ferrite [38,39]. The possible technical applications of the $Co_xMn_{1-x}Fe_2O_4$ spinel ferrites were studied in the papers [28,40].

However, despite a big number of the papers devoted to studies of the $Co_xMn_{1-x}Fe_2O_4$ MNPs, the obtained results are contradictory, for example, in determining a structure transformation degree (inversion parameter) of the nanoparticles. The published experimental data are often inconsistent. There is wide scattering of data on magnetic properties of the particles, even in case of the MNPs of the same size and composition. Such a wide dispersion is usually attributed to a presence of distributions in terms of sizes and a shape, stoichiometric gradients, inter-particle interactions and structure flaws, which greatly depend on a synthesis procedure and it is difficult to define their contributions. In application of the $Co_xMn_{1-x}Fe_2O_4$ MNPs for the magnetic hyperthermia, it was established that similar MNPs can exhibit strong differences in their heating efficiency due to internal flaws correlated to the synthesis method or due to differences in a local spin structure. In these cases it is difficult to explain a dependence of the physical properties on the synthesis methods, also because it is necessary to compare the magnetic responses of the differently produced MNPs based on a comprehensive structural and magnetic characteristic [10,23,39,40]. Thus, it is expedient to carry out the studies of the $Co_xMn_{1-x}Fe_2O_4$ MNPs with using different well-recommended methods, such as, the Mössbauer spectroscopy.

The present paper provides results obtained in the study of the structural and magnetic properties of the

$Co_xMn_{1-x}Fe_2O_4$ SF MNPs depending on a content of the Co^{2+} ions, which has been carried out to develop MNP research for biomedicine applications as started in the paper [10].

2. Materials and methods

2.1. Synthesis of $Co_xMn_{1-x}Fe_2O_4$ MNPs ($x = 0$, 0.2, 0.3, 0.4, 0.5, 0.6, 0.8 and 1.0)

The studied $Co_xMn_{1-x}Fe_2O_4$ MNPs of the mixed SF (where $0 \le x \le 1.0$) were synthesized by a simple method of coprecipitation in a water medium, as it was described in the paper [10]. The synthesis of each composition of the $Co_xMn_{1-x}Fe_2O_4$ MNP requires an estimated quantity of the salts $MnCl_2$, $CoCl_2$, $_6H_2O$ and $FeCl_3$ to be dissolved in 200 ml of deionized water. The produced mixture was heated to 80°C and the 1 N NaOH solution was dropped into it, continuously mixing it, to get pH to 12−13. The solution mixture was heated at 85°C during 1 h and cooled down to the room temperature. The synthesized MNPs were filtered and then flushed several times with deionized water, dried under an infrared lamp and the produced particles were used for the studies. The MNP composition was analyzed by means of SEM-EDS, and it was found that the composition of the produced $Co_xMn_{1-x}Fe_2O_4$ MNPs agrees with used synthesis components ($x = 0$, 0.2, 0.3, 0.4, 0.5, 0.6, 0.8 and 1.0).

2.2. Methods of characterization of the $Co_xMn_{1-x}Fe_2O_4$ MNPs

The phase composition of the synthesized $Co_xMn_{1-x}Fe_2O_4$ MNPs and crystallite sizes were determined by an X-ray diffraction profile using the XRD Shimadzu-6100 powder diffractometer with the Cu-$K\alpha$ radiation and the wave length of 1.542 Å. The transmission electron microscope (TEM) FEI Titan Themis 300 kV was used to obtain light field images and electron diffraction images on the selected areas. The magnet measurements in the constant magnetic field were carried out using the vebrating sample magnetometer in Quantum Design meter system. The Raman spectra of the MNP pills were obtained by means of the NOST Raman-scattering spectrometer using the solid-state laser with diode pumping, which operates at the wave length of 532 nm and a charge-coupled detector.

Due to high sensitivity to the nuclear hyperfine interactions, the Mössbauer spectroscopy is an effective method for the MNP studies and allows studying a dependence of the MNP properties on a particle size, a temporary measurement window and a magnetic anisotropy [41–45]. The important advantage of the Mössbauer spectroscopy is unambiguous identification of iron oxides, which have very close values of the crystal lattice constants, which is unavailable in other procedures. That is why the Mössbauer spectroscopy allows definitely determining the phase state, the ion distribution across the nonequivalent positions, the magnetic structure and the hyperfine interactions in iron-containing materials [41–45]. If the time of oscillations of a MNP magnetization direction exceeds 10^{-8} s, then the Mössbauer spectrum has an evident Zeeman sextuplet indicating a magnetically-ordered state of the substance. When the fluctuation time is below 10^{-8} s, the time-averaged hyperfine field being created by the magnetic moment, becomes zero during the Mössbauer measurements and, therefore, the Mössbauer spectrum will consist a doublet or a single line, which corresponds to a paramagnetic or superparamagnetic state of the substance.

The Mössbauer studies of the magnetic structure and the phase state of the synthesized $Co_xMn_{1-x}Fe_2O_4$ MNPs were carried out by the spectrometer with recording gamma-rays from the Co^{57}(Rh) source in a sample transmission geometry. The scale was calibrated by α-Fe foil of the thickness of 6 *mu*m at room temperature. The experimental Mössbauer spectra (MS) of the $Co_xMn_{1-x}Fe_2O_4$ MNPs were mathematically processed by a special software application [46], which describes spectrum lines by Lorentz-shaped peaks using the method of least squares. Divergence of the theoretical values of the HFI parameters is determined from the statistical deviations. The software procedure of chi-square functional minimization (χ^2) include searching for optimal values of the parameters, particularly, a width, intensities and positions of the spectrum lines. Using the positions of the spectrum lines, the parameters of the hyperfine interactions (HFI) are calculated: IS — the isomer shift of the Mössbauer lines, QS — the quadrupolar splitting, H_{eff} — the effective magnetic hyperfine field.

3. Results and discussion

3.1. X-ray diffraction patterns of the $Co_xMn_{1-x}Fe_2O_4$ MNPs ($x = 0$, 0.2, 0.4, 0.6, 0.8 and 1.0)

Fig. 1, *a* shows the X-ray diffraction patterns (XD) of the $Co_xMn_{1-x}Fe_2O_4$ MNPs at room temperature. The obtained X-ray diffraction patterns are similar to those published in the literature for $CoFe_2O_4$ in [19,22], for $Mn_{1-x}Co_xFe_2O_4$ in [11,14,32] and for $MnFe_2O_4$ in [19]. The narrow widths of the XD lines indicate a high quality of particle crystallization, while their positions mean formation of a face-centered cubic structure of the spinel. No additional peaks belonging to the secondary phases have been found on the X-ray diffraction patterns of the samples under study. Calculated values of the elementary cell parameters for $CoFe_2O_4$ are 8.3891 Å, while for $MnCoFe_2O_4$ — 8.4889 Å, which agree with the values for the bulk analogs 8.391 Å for $CoFe_2O_4$ (JCPDS № 22-1086) and 8.499 Å for $MnFe_2O_4$ (JCPDS № 10-0319). The calculated values of the lattices constant for the $Co_xMn_{1-x}Fe_2O_4$ solid solution decrease with increase in the quantity of the Co^{2+} ions, since the Co^{2+} ion radius is less than that of the Mn^{2+} ion. The obtained values of the lattice parameter for the $MnFe_2O_4$

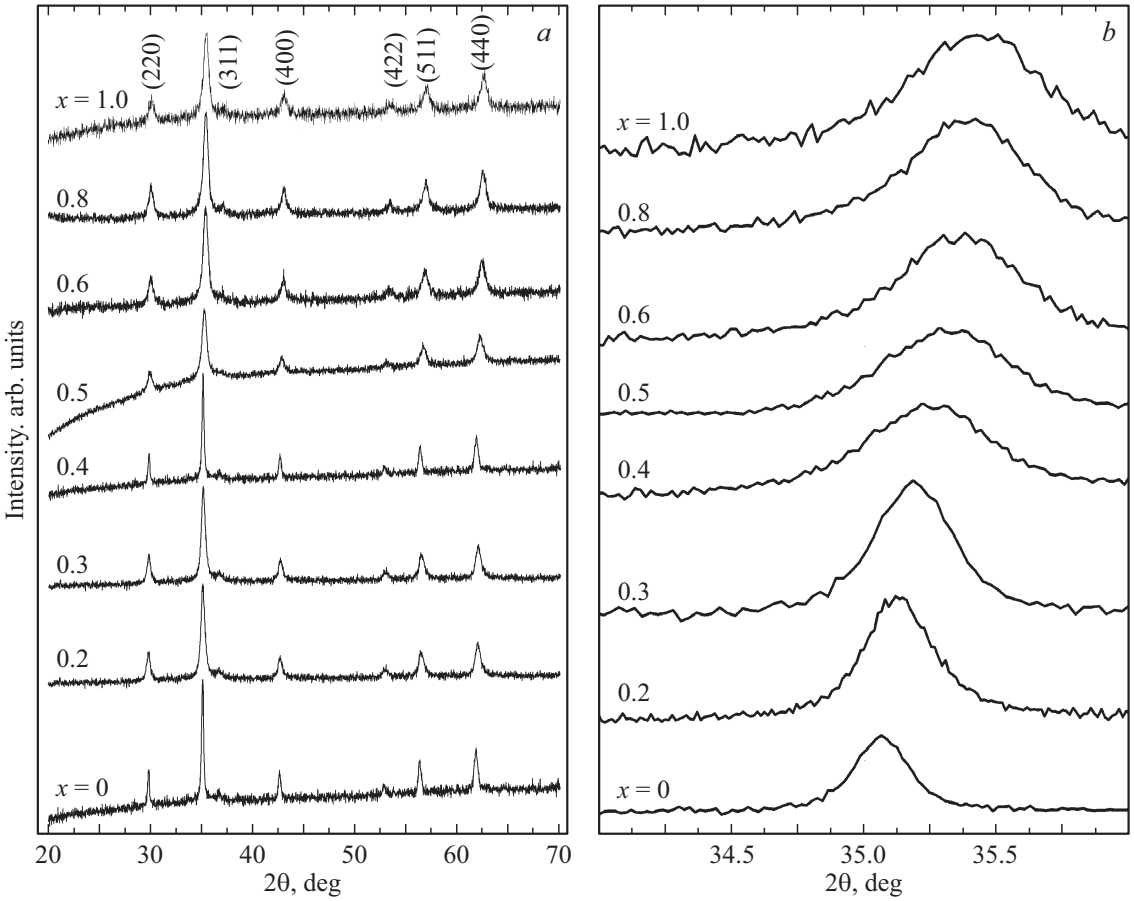

Figure 1. *a* — X-ray diffraction patterns of the $Co_xMn_{1-x}Fe_2O_4$ MNPs ($0 \le x \le 1.0$). *b* — the change inthe position of the peak of maximum intensity (311) as a function of cobalt content.

(8.4889 Å) and $CoFe_2O_4$ (8.3891 Å) nanoparticles agree with data of the papers (see, for example, [47]).

Fig. 1, *b* shows the dependence positions of the XD line of maximum intensity (311) depending on the Co concentration. As the Co ion concentration is increasing, the positions of the XD lines are shifting towards a higher diffraction angle, which has been also observed in the study [14]. The widths of the XD line (Fig. 1, *b*) belonging to $MnFe_2O_4$ are substantially smaller than for $CoFe_2O_4$, indicating that the average sizes of the $CoFe_2O_4$ MNPs are smaller. Using the XD data and the Scherrer formula, the sizes of the $Co_xMn_{1-x}Fe_2O_4$ crystallites have been calculated, which are shown in Fig. 2 as function of the Co concentration. Fig. 2 shows that the average size of the $MnFe_2O_4$ crystallites of 34.86 nm is sharply decreasing during the substitution of the Co ions to reach the value of 14.99 nm for $CoFe_2O_4$. The evident difference of the sizes of the $MnFe_2O_4$ and $CoFe_2O_4$ particles can be attributed to a different diffusion rate of the Co^{2+} and Mn^{2+} ions in the water medium.

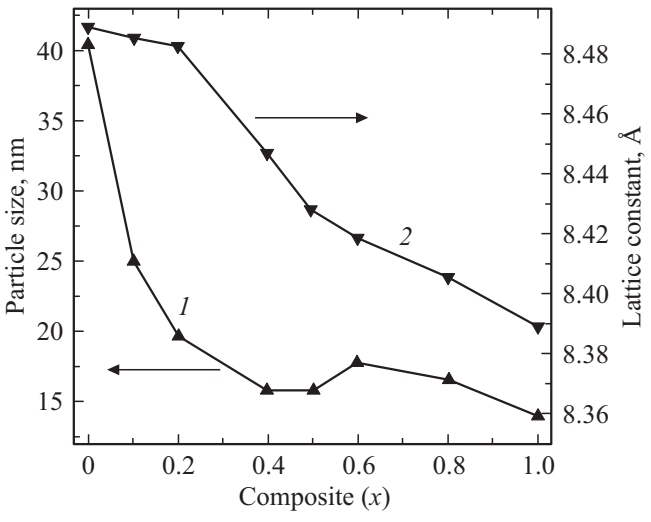

Figure 2. Size change of the crystallites $Co_xMn_{1-x}Fe_2O_4$ (*1*), the lattice constant (*2*) dependence on the content of the Co ions (x).

3.2. Raman spectra of the $Co_xMn_{1-x}Fe_2O_4$ MNPs (x = 0.0, 0.2, 0.3, 0.4, 0.5, 0.6, 0.8 and 1.0)

The Raman spectroscopy is a non-destructive and highly-efficient experimental method of directly studying the lattice dynamics and structural and vibratory properties in different types of the materials [48]. Fig. 3 shows the Raman spectra

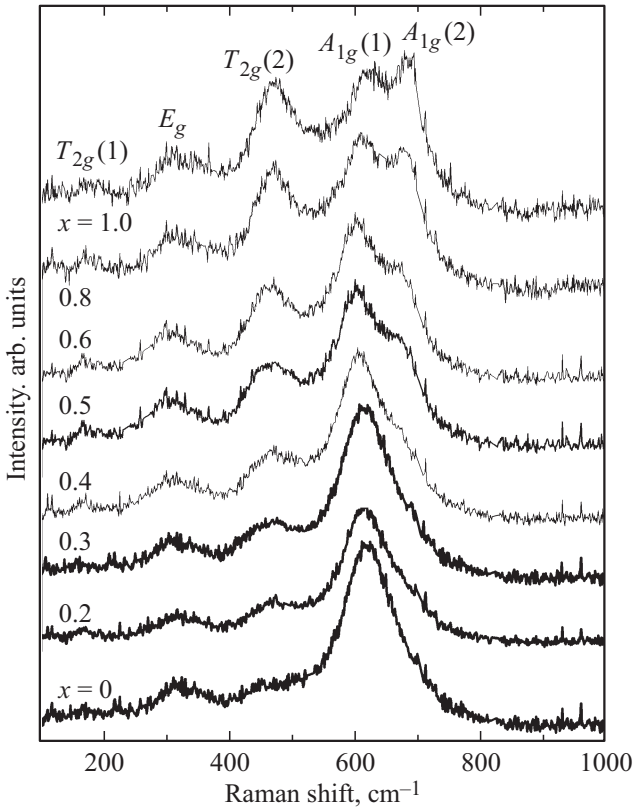

Figure 3. Raman spectra of the $Co_xMn_{1-x}Fe_2O_4$ MNPs ($0 \le x \le 1.0$) (correspondence of the peaks is shown in the figure).

(RS) of the synthesized $Co_xMn_{1-x}Fe_2O_4$ MNPs, which are obtained by means of the spectrometer with the solid-state laser of the wave length of 532 nm and with recording the data by a highly-sensitive semiconductor charge-coupled detector. The laser power was optimized so that the ferrite particles do not oxidize with forming the Fe_2O_3 phase [10].

Occupation of the octahedral and tetrahedral positions of the crystal structure is a factor on which the line positions and their intensities in RS depend, whose analysis has shown the following. The Raman-scattering spectra of light indicate a inverse spinel structure of the $CoFe_2O_4$ nanoparticles. For the composition with $x = 0$, there is an evident spectrum, whose line positions coincide with the positions observed for the $MnFe_2O_4$ SFs [49].

The spectrum of the composition of $x = 0.4$ has evident splitting of the A1g line,and the splitting increases with the increase in the Co^{2+} quantity in the $Co_xMn_{1-x}Fe_2O_4$. It means that the input of the Co^{2+} ions (at $x \ge 0.2$) led to redistribution of the (Co^{2+}, Mn^{2+}, Fe^{3+}) cations in $Co_xMn_{1-x}Fe_2O_4$. The analysis of the line intensity ratio in the spectra for the compositions of $x = 1.0$ and 0.8 has shown that Co^{2+} and Fe^{3+} are uniformly distributed in the tetrahedral positions, whereas for $x = 0.4$ and 0.6 the intensity ratio indicates that there are less Fe^{3+} ions in the tetrahedral positions [10]. This is due to the fact that the Mn^{2+} ions prefer the tetrahedral position by displacing the Fe^{3+} ions. The Raman spectra of the Fe_3O_4 powders have an evident line at 292 cm^{-1}, which is absent at the spectra of the $CoFe_2O_4$ and $MnFe_2O_4$ spinels [50]. The spectra of the $Co_xMn_{1-x}Fe_2O_4$ MNPs under study have no evident line at 292 cm^{-1}, and thus we can state with certainty that there is no Fe_3O_4 phase in the MNPs under study, and no line indicating existence of other impurity phases. It should be noted that the obtained Raman spectra of the MNPs and $MnFe_2O_4$ and $Co_xMn_{1-x}Fe_2O_4$ (Fig. 3) are similar to those specified in [49] and [48,51], respectively.

3.3. Mössbauer spectroscopy of the $Co_xMn_{1-x}Fe_2O_4$ MNPs

Important information about the phase composition, local electron configurations, magnet interactions and magnetic relaxation phenomena of the nanosized systems can be provided by the Mössbauer spectroscopy. The experimental Mössbauer spectra (MS) of ^{57}Fe MNPs of the $Co_xMn_{1-x}Fe_2O_4$ ferrite recorded at the room temperature are shown in the Fig. 4. The experimental values are the dotts in the Fig. 4, while the model spectra, which are obtained in the mathematical processing of the experimental Mössbauer spectra by means of the program [46], are shown by the solid lines. Good compliance of the used models with the experimental Mössbauer spectra of the $Co_xMn_{1-x}Fe_2O_4$ MNPs is confirmed by minimum values of the difference between the model and experiment values, which are shown above each spectrum and by the values χ^2 within 1.0−1.2. The parameters of hyperfine interactions (HFI), which are calculated based on the positions of the Zeeman lines in Mössbauer spectra of the $Co_xMn_{1-x}Fe_2O_4$ MNPs are shown in the table. The values of the isomer shifts (IS) are given relative to the α-Fe metal foil. The impurity phases of the iron oxides should appear distinctly on the Mössbauer spectra of $Co_xMn_{1-x}Fe_2O_4$ as additional Zeeman sextuplets (ZS) or doublets with different HFI parameters. The detection limit of the secondary phase is about 1−3 at.% of the iron and any phase even with such an iron quantity can be easily determined from the Mössbauer spectra. The analysis of the experimental Mössbauer spectra of the $Co_xMn_{1-x}Fe_2O_4$ MNPs has not revealed any additional lines. Thus, there are no impurity phases in the MNPs under study, which coincides with results of XD and Raman studies.

The Mössbauer spectra of the $Co_xMn_{1-x}Fe_2O_4$ MNPs (Fig. 4) substantially differ in the shape from the spectra of the macroscopic crystals (for example, [14,52–56]). As it is clear from Fig. 4, the experimental Mössbauer spectravconsist in the ZS wide lines on whose background with reduction of the quantity of the Co ions there are within the zero rate range evident doublet lines, whose intensity increases with increase in the concentration of the Mn ions. It should be noted that the obtained Mössbauer spectra of the $Co_xMn_{1-x}Fe_2O_4$ MNPs (Fig. 4) are similar to those observed at $x = 0$ (for $MnFe_2O_4$) in [8,18,19],

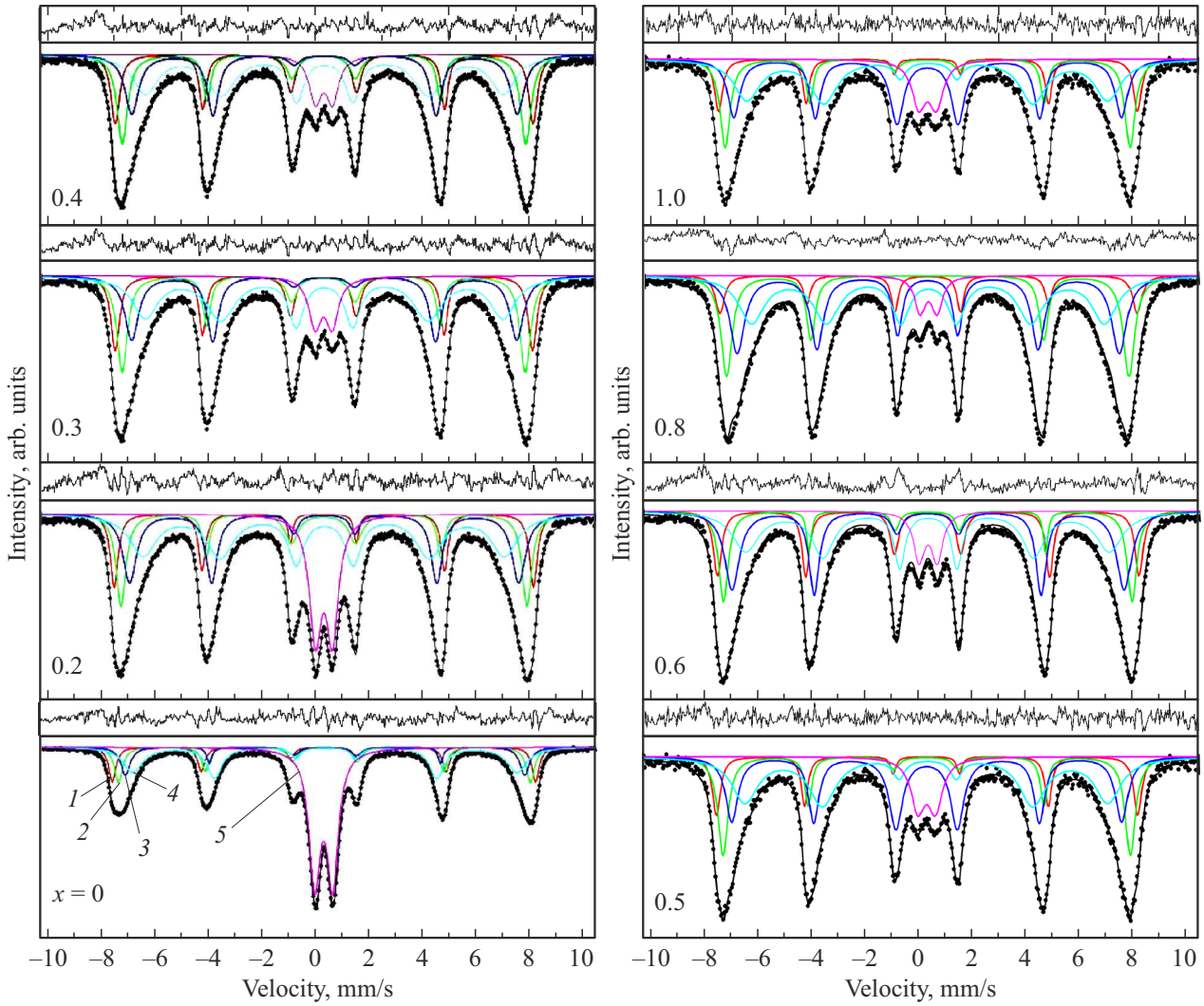

Figure 4. Mössbauer spectra of the $Co_xMn_{1-x}Fe_2O_4$ MNPs obtained at the room temperature. The experimental values are the dotts, while the model sextuplets are shown by solid color lines: The sublattices A are designated by a number *1*, while the sublattices B1, B2 and B3 — *2, 3* and *4*, respectively, the doublet — *5* (in accordance with the colors).

and at $x = 1.0$ (for $CoFe_2O_4$) in [57], as well as for the $Co_xMn_{1-x}Fe_2O_4$ particles in [4,9,18,58].

The Mössbauer spectroscopy allows reliably identifying the spectrum lines belonging to the Fe^{2+} and Fe^{3+} ions by their chemical shifts making up $\sim 0.2-0.5$ mm/s for Fe^{3+} and $\sim 0.9-1.1$ mm/s for Fe^{2+} [59]. However, for the spinel ferrite MNPs the IS values belonging to the iron ions in the high-spin state Fe^{3+} are usually within the range of 0.3−0.6 mm/s. There are not higher values of the chemical shifts (from 0.9 to 1.1 mm/s), which belong to the Fe ions in the low-spin state Fe^{2+} [59]. As it is clear from the table, the values are within 0.3−0.5 mm/s. It means that the $Co_xMn_{1-x}Fe_2O_4$ MNPs under study have only the iron ions in the high-spin state Fe^{3+}. That is why a group of the sextuplets observed at the Mössbauer spectra of $Co_xMn_{1-x}Fe_2O_4$ (Fig. 4) are due to to the iron ions occupying the A and B sublattices, was determined by a value of the effective magnetic fields, as it is well known that in the MFe_2O_4 spinel ferrites (where M — metal ions) the hyperfine magnetic field of the Fe ions is bigger in the A sites than in the B sites [14,52.56].

The satisfactory description by the χ^2 criterion of the Mössbauer spectra of $Co_xMn_{1-x}Fe_2O_4$ MNPs was obtained by using four Zeeman sextuplets and one doublet. The first sextuplet with the maximum effective magnetic hyperfine field corresponds to the Fe ions occupying the tetrahedral A positions, while the three others designated as B1, B2 and B3 correspond to the Fe ions in the octahedral B positions Table 1). The formation of such spectra in the spinel ferrites is observed in the studies [60–62] and attributed for the first time to random distributions of the cations in the A sublattice. The presence of the three different cations (iron, cobalt and manganese) in the samples under study significantly increases the chances of random distribution of these cations, thereby leading to formation of several octahedral positions which differ in the occupation. The

Values of the widths of the first and sixth lines (G) of the Zeeman splitting as well as the isomer shifts (IS), the quadrupolar splittings (QS), the effective magnetic hyperfine fields (H_{eff}) and the areas of the Zeeman sextuplets (S) for the Fe ions in the tetrahedral (A) and octahedral (B) positions and of the doublets (D) in the $Co_xMn_{1-x}Fe_2O_4$ MNPs depending on a composition of the Co ions (x).

X	Components	G (mm/s)	IS (mm/s)	QS (mm/s)	H_{eff} (T)	S (%)
1.0	A	0.341+/-0.033	0.339+/-0.004	0.035+/-0.008	48.85+/-0.06	10
	B1	0.453+/-0.042	0.309+/-0.003	0.018+/-0.006	47.27+/-0.05	18
	B2	0.632+/-0.061	0.319+/-0.002	0.001+/-0.005	45.24+/-0.08	28
	B3	1.154+/-0.043	0.334+/-0.005	0.023+/-0.010	42.05+/-0.18	41
	D1	0.631+/-0.064	0.334+/-0.013	0.662+/-0.032	–	4
0.8	A	0.391+/-0.033	0.329+/-0.003	0.028+/-0.007	48.35+/-0.07	9
	B1	0.512+/-0.037	0.309+/-0.002	0.013+/-0.004	46.62+/-0.04	20
	B2	0.670+/-0.050	0.324+/-0.002	0.022+/-0.004	44.26+/-0.07	31
	B3	1.134+/-0.033	0.338+/-0.005	0.024+/-0.009	40.87+/-0.14	36
	D1	0.478+/-0.020	0.348+/-0.005	0.630+/-0.011	–	4
0.6	A	0.361+/-0.014	0.330+/-0.001	0.019+/-0.003	48.64+/-0.03	17
	B1	0.426+/-0.021	0.313+/-0.002	0.013+/-0.003	47.15+/-0.03	15
	B2	0.665+/-0.028	0.328+/-0.002	0.011+/-0.003	45.24+/-0.04	28
	B3	1.190+/-0.031	0.332+/-0.004	0.028+/-0.007	42.00+/-0.12	33
	D1	0.500+/-0.012	0.337+/-0.003	0.674+/-0.007	–	7
0.5	A	0.353+/-0.045	0.331+/-0.004	0.020+/-0.009	48.66+/-0.09	17
	B1	0.455+/-0.071	0.317+/-0.005	0.017+/-0.009	47.05+/-0.09	18
	B2	0.561+/-0.092	0.329+/-0.004	0.004+/-0.009	45.03+/-0.14	25
	B3	1.160+/-0.066	0.342+/-0.010	0.042+/-0.019	41.93+/-0.28	34
	D1	0.633+/-0.041	0.328+/-0.009	0.656+/-0.020	–	9
0.4	A	0.387+/-0.013	0.323+/-0.001	0.018+/-0.002	48.43+/-0.03	17
	B1	0.472+/-0.024	0.323+/-0.002	0.011+/-0.003	46.79+/-0.03	20
	B2	0.621+/-0.035	0.344+/-0.002	0.002+/-0.003	44.69+/-0.05	21
	B3	1.117+/-0.023	0.348+/-0.003	0.012+/-0.006	41.53+/-0.10	35
	D1	0.554+/-0.013	0.328+/-0.003	0.638+/-0.007	–	7
0.3	A	0.387+/-0.013	0.323+/-0.001	0.018+/-0.002	48.43+/-0.03	17
	B1	0.472+/-0.024	0.323+/-0.002	0.011+/-0.003	46.79+/-0.03	20
	B2	0.620+/-0.035	0.344+/-0.002	0.002+/-0.003	44.69+/-0.05	21
	B3	1.118+/-0.023	0.348+/-0.003	0.012+/-0.006	41.53+/-0.10	35
	D1	0.554+/-0.013	0.328+/-0.003	0.638+/-0.007	–	7
0.2	A	0.345+/-0.021	0.320+/-0.002	-0.017+/-0.004	48.60+/-0.05	12
	B1	0.436+/-0.043	0.328+/-0.003	-0.017+/-0.005	47.06+/-0.06	18
	B2	0.620+/-0.054	0.344+/-0.003	-0.000+/-0.005	45.11+/-0.09	21
	B3	1.181+/-0.043	0.345+/-0.005	0.036+/-0.010	41.88+/-0.19	33
	D1	0.537+/-0.009	0.339+/-0.002	0.635+/-0.004	–	16
0.0	A	0.315+/-0.012	0.318+/-0.003	-0.005+/-0.006	49.80+/-0.03	12
	B1	0.360+/-0.029	0.345+/-0.002	0.006+/-0.004	47.69+/-0.04	15
	B2	0.420+/-0.031	0.361+/-0.003	-0.005+/-0.006	46.23+/-0.04	10
	B3	0.892+/-0.021	0.375+/-0.003	0.029+/-0.005	42.51+/-0.09	25
	D1	0.254+/-0.035	0.478+/-0.006	0.709+/-0.008	–	2
	D2	0.498+/-0.004	0.318+/-0.004	0.672+/-0.001	–	35

values of the hyperfine field of the A sublattice of the SF depend on a quantity of the cations in another sublattice, particularly, the B sublattice. Via the superexchange interaction A–B, these cations determine the hyperfine fields of the ions of the A positions, which have twelve adjacent neighbors in the B positions and, therefore, depend less on a random distribution of the cations in the B points. However, for the B positions, the adjacent neighbors include only six cations in the A positions and the random cation distribution across these positions is much more important for the hyperfine fields of the Fe ions of the B sublattice. In other words, the change in the cation distribution across the

B positions affects the A positions only by 1/12, whereas the change in the cation distribution across the A positions leads to the changes in the B sublattice by 1/6 [62].

Thus, the Zeeman sextuplets with the biggest effective fields belong to the iron ions occupying the A sublattice in the crystal lattice of $Co_xMn_{1-x}Fe_2O_4$ SF MNPs, while the other sextuplets are related to the Fe ions in the B positions. That is why the B3 sextuplet with the lowest values of the hyperfine field and large widths of the lines also occurs due to random ion distribution. Moreover, a large surface-to-volume ratio of the nanoparticles leads to a much bigger role of the iron ions located in the surface layer of the particles. That is why the B3 sextuplet can be contributed by the surface Fe ions, which have a smaller number of magnetic bonds [29] and/or a less biased state of their magnetic moments [62–64].

As it is clear from the Fig. 4, at $x = 1.0$, the Zeeman sextuplet's background has evident lines of small intensity within the velocity rate range, which belong to the quadrupolar doublet. The doublet intensity increases with the increase in the number of the Mn ions. At $x = 0$ ($MnFe_2O_4$), there are evidently two doublets, whose total area can take up to 37% of the whole area of the spectrum lines. The formation of Zeeman and doublet lines on the Mössbauer spectra is typical for superparamagnetic relaxation of the MNPs and can be explained by taking into account two populations: one is based on bigger particles, whose magnetic moments slowly fluctuate and the Zeeman sextuplet is observed on the Mössbauer spectra, while the other — on smaller particles with less relaxation time of the moments, which form the quadrupolar doublet on the Mössbauer spectra.

The QS values (Table 1) of the nonequivalent positions of the iron ions in the studied $Co_xMn_{1-x}Fe_2O_4$ SF MNPs within the experiment error are close to zero (except for IS for the doublets), thereby meaning maintaining the cubic symmetry between the Fe^{3+} ions and its environment. The value of the QS doublets below 0.8 mm/s indicates that in the $Co_xMn_{1-x}Fe_2O_4$ MNPs of smaller sizes, the Fe ions are also in the high-spin state Fe^{3+}, as for the Fe^{2+} ions in the low-spin state the QS value is significantly higher.

The change of the hyperfine magnetic field (H_{eff}) of the different sextets depending on the substitution value is shown Table and in the Fig. 5. As it is clear from Fig. 5, H_{eff} of the B ions of the sublattice reduces at $x = 0.2$, and further increase in the Mn^{2+} quantity leads to insignificant changes, reaching the maximum value of 49.80 T at $x = 0$. It can be concluded therefrom that when increasing of the Mn concentration Mn impurity the magnetization is changing not only by simple substitution of the Fe^{3+} ions with non-magnetic Mn ions, but by a more complex process as well.

The table shows the IS values for the Fe^{3+} ions in the tetrahedral A and octahedral B positions in the $Co_xMn_{1-x}Fe_2O_4$ MNPs depending on the substitution value. As it is clear from the table, the IS values of the Fe ions in the B positions almost coincide with the IS for the A iron ions and do not depend on the Mn ion concentration,

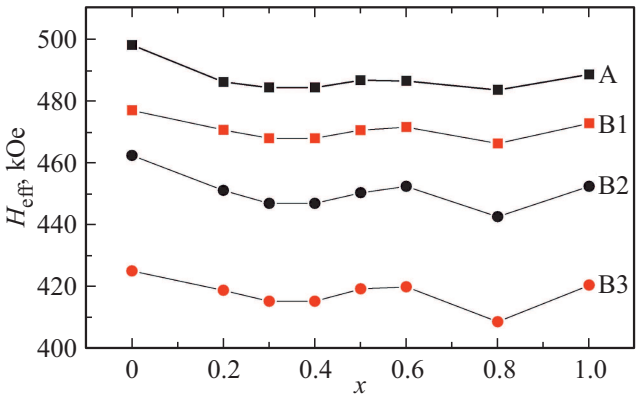

Figure 5. Dependences of the effective magnetic fields on the iron ion nuclei, which occupy different sublattices in the $Co_xMn_{1-x}Fe_2O_4$ MNPs, depending on the substitution value of the Co ions.

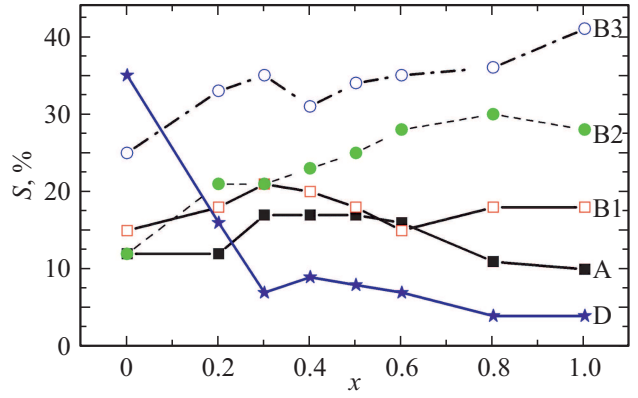

Figure 6. Dependences of the areas of the spectrum lines of the different sublattices in the $Co_xMn_{1-x}Fe_2O_4$ MNPs, depending on the substitution value.

thereby meaning insensitivity of the s-electrons of the Fe^{+3} ions to the Mn quantity. The range of the IS values for the A and B positions is within 0.3–0.5 mm/s, indicating that in the ferrites under study the iron is in the valence of the high-spin configuration Fe^{3+}.

As it is clear from the table, the widths of the lines of the sextuplets of the Fe ions in the A positions almost do not depend on the quantity of the Mn ions in the solid solution, but their values are less than for the Fe ions in the B positions for the whole range of substitution by the Co^{2+} ions. The line widths, corresponding to the ions in the A and B sublattices, increase in the ions in the B points from 0.45 to 1.19 mm/s, while for the A sublattice they vary from 0.31 to 0.39 mm/s. Increased line widths of the Fe ions in the B positions can be correlated to the distribution of the Mn^{2+} ions in the environment of the Fe^{3+} ions occupying the B positions. The line widths of the doublets are within 0.48–0.63 mm/s (Table), which is close to the values of 0.6 and 0.7 mm/s, which are obtained for the $MnFe_2O_4$ doublet in papers [9,65].

The dependences of the areas of the spectrum lines for the $Co_xMn_{1-x}Fe_2O_4$ SF MNPs on the substitution value are given in Table and the Fig. 6. They clearly show that the line areas of the B2 and B3 sextuplets for the $MnFe_2O_4$ ($x = 0$) are smaller than for the $CoFe_2O_4$ ($x = 1$). This can be attributed to the fact that the $CoFe_2O_4$ particles are smaller in sizes than the $MnFe_2O_4$ particles and the contribution of the Fe ions in the surface layer of the $CoFe_2O_4$ particles is bigger. The doublet area for the $MnFe_2O_4$ is significantly higher than for the $CoFe_2O_4$, which is attributed to the lower temperature of the magnetic blocking of the $MnFe_2O_4$ particles in comparison with the $CoFe_2O_4$.

The values of the areas of the spectrum lines of the sextuplets and doublets (S in Table) in the Mössbauer spectra (Fig. 4) allowed determining a relative quantity of the magnetic and paramagnetic phases in the MNPs under study. As the concentration of Mn ions is increasing, the line area ratio of the sextuplets and doublet in the Mössbauer spectra of the $Co_xMn_{1-x}Fe_2O_4$ MNPs is decreasing. Therefore, with decrease in the content of the Co ions, the blocking temperature (BT) value of the $Co_xMn_{1-x}Fe_2O_4$ MNPs is decreasing, but failing to reach the room temperature at $x = 0$.

3.4. Distribution functions of effective magnetic hyperfine fields P(H_{eff})

No distinct resolution of the sextuplets in the Mössbauer spectra of the $Co_xMn_{1-x}Fe_2O_4$ MNPs under study substantially impedes using the distinct physical model for describing such spectra. That is why the experimental Mössbauer spectra of the $Co_xMn_{1-x}Fe_2O_4$ MNPs have been used by the dedicated software application [46] to recover probability distribution functions of the magnetic hyperfine fields fields (P(H_{eff})), which are shown in the Fig. 7. The obtained functions P(H_{eff}) differ from P(H_{eff}) of the SF macrocrystals, which evidently have only two maximums belonging to the iron ions in the two nonequivalent sublattices. The functions P(H_{eff}) of the $Co_xMn_{1-x}Fe_2O_4$ MNPs (Fig. 7) have evident maximums within the two H_{eff} ranges: from 0 to 5 T and from 32 to 53 T. The range from 0 to 5 T corresponds to the doublet lines on the Mössbauer spectra, which are related to a fraction of the particles in the paramagnetic state and whose availability probability is increasing, as it is clear from Fig. 7, as the quantity of Mn ions is increasing in the $Co_xMn_{1-x}Fe_2O_4$ MNPs. The curves P(H_{eff}), which are observed within the range from 32 to 53 T (Fig. 7), are related to the ZS lines, which, however, have different environments. The separation of the functions P(H_{eff}) into the two areas (Fig. 7) means that there are two groups of particles in the synthesized $Co_xMn_{1-x}Fe_2O_4$ MNPs: fine particles, which correspond to H_{eff} within the range from 0 to 5 T, and large MNPs, which are described by the functions P(H_{eff}) within the range from 32 to 53 T. As it is clear from Fig. 7, the curves obtained for $x + 0$ and $x = 1.0$ are narrower than the others and distributed within the range of 30–53 T. Besides,

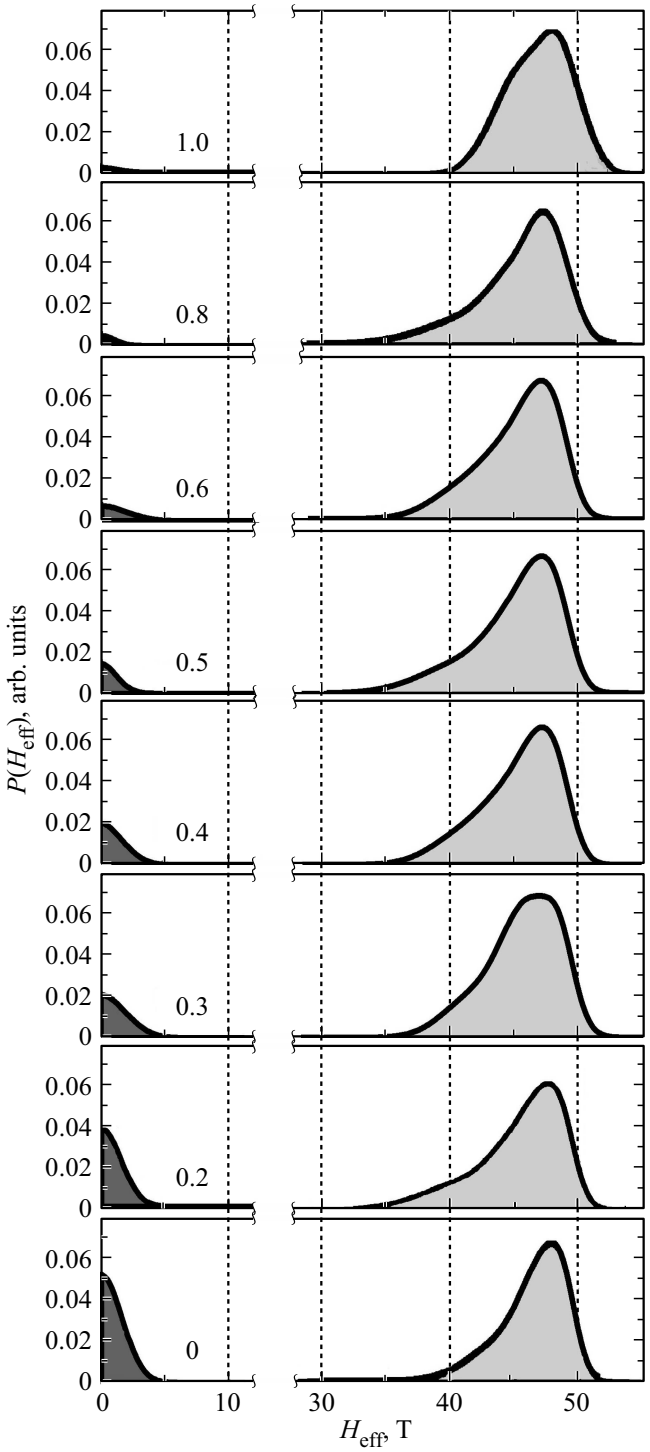

Figure 7. Distribution functions P(H_{eff}) recovered from the experimental Mössbauer spectra of the $Co_xMn_{1-x}Fe_2O_4$ MNPs (Fig. 4) by means of the software application [46].

at $x = 1.0$ the curve P(H_{eff}) can be distinguished to have two maximums belonging to the iron ions in the A and B1 positions. At the substitution values within the range x from 0.2 to 0.8, the functions P(H_{eff}) have evident long „tails“ directed towards reduction of H_{eff}. It means that

when introducing the Co ions into the MNPs, there are nonequivalent positions being formed, which are correlated not only to the change of the environment of the Fe resonant ions, but to varying properties of all the surrounding ions, thereby leading to formation of a number of the tetrahedral coordinations with insignificantly different parameters.

Detailed analysis of the Mössbauer spectra (Fig. 4) and the distribution of the fields $P(H_{eff})$ has shown that in order to satisfactorily describe the Mössbauer spectra of the $Co_xMn_{1-x}Fe_2O_4$ by the χ^2 criterion, it is necessary to use the superposition of at least four partial Zeeman sextuplets. That is why in order to get quantitative information on values of the parameters of hyperfine interactions of the Zeeman sextuplets and doublets, the experimental Mössbauer spectra of the $Co_xMn_{1-x}Fe_2O_4$ MNPs (Fig. 4) have been processed by the superposition model of the four partial sextuplets and doublet. Some differences in the values of H_{eff} (Fig. 7) and the values of the cells in the table are due to existence of different coordinations (types) of the Fe atom environment in the $Co_xMn_{1-x}Fe_2O_4$ MNPs under study. Thus, features of the functions $P(H_{eff})$ (Fig. 7) reflect a complex magnetic structure of the $Co_xMn_{1-x}Fe_2O_4$ MNPs under study, which can not be attributed only to the change of the distribution of ions surrounding the iron ions during inputting the Co ions, and it is necessary to take into account a state of the environment ions, too.

Analysis of the experimental Mössbauer spectra of the $Co_xMn_{1-x}Fe_2O_4$ MNPs and the published results of Mössbauer studies allow evaluating the sizes of the MNPs under study. Thus, the papers [9,18,19,24] provide results of the Mössbauer studies of the $MnFe_2O_4$ MNPs with the sizes from 3 nm to 98 nm. The studies of the $CoFe_2O_4$ MNPs of the different sizes are provided in the papers [66–71], while the paper [27] provides the Mössbauer data for the $Co_xMn_{1-x}Fe_2O_4$ particles of the sizes of 8 nm (for $x = 0.1$) and 13 nm (for $x = 0.5$). The comparison of the Mössbauer spectra data with the published data allows concluding that the sizes of the $Co_xMn_{1-x}Fe_2O_4$ particles under study change from 25 nm to 12 nm when being substituted by the Co ions from $x = 0$ to $x = 1.0$.

4. Conclusion

For the first time, the systematic studies of the $Co_{1-x}Mn_xFe_2O_4$ MNPs have been carried out in dependence on the Mn ion concentration ($x = 0.0$, 0.2, 0.3, 0.4, 0.5, 0.6, 0.8, 1.0), which have been synthesized using a simple method of coprecipitation. The structural and morphology properties of the MNPs have been studied by means of the X-ray diffraction (XD), the transmission electron microscopy, the Raman and Mössbauer spectroscopy. The XD structural analysis and the data of the Raman and Mössbauer spectroscopy confirm formation of the $Co_{1-x}Mn_xFe_2O_4$ single-phase ferrite with the cubic structure of the inverce spinel ferrite (the spatial group Fd3m) within the whole range of the substitution by the Co ions. The Raman-scattering method has established that the $MnFe_2O_4$ MNPs are structured as a normal spinel and when being doped by the Co^{2+} ions, the Co^{2+} and Fe^{3+} cations are redistributed between tetrahedral and octahedral positions and the structure converts to the mixed ferrite. Based on the X-ray diffraction data, it is established that the average size of the $MnFe_2O_4$ ($x = 0$) crystallites is ~ 35 nm and the particles decrease in size with increase in the Co quantity, reaching ~ 15 nm for $CoFe_2O_4$ ($x = 1.0$). The Mössbauer spectroscopy data indicate that the sizes of the $Co_{1-x}Mn_xFe_2O_4$ MNPs change within the range from 12 to 25 nm when the value of substitution with the Co ions is decreasing from $x = 1.0$ to $x = 0$, which insignificantly differs from the X-ray diffraction results.

The Mössbauer spectra of the $Co_{1-x}Mn_xFe_2O_4$ MNPs consisting the Zeeman sextuplet with the wide lines, whose background has an evident quadrupolar doublet, indicate a typical superparamagnetic behavior of the $Co_{1-x}Mn_xFe_2O_4$ MNPs. The Mössbauer spectra type is explained based on the model of the two populations: one — large particles, whose sizes are bigger than a critical value, wherein the magnetic moments vibrate with the frequency below the Larmor precession frequency, and the Mössbauer spectra have the Zeeman sextuplets; the other population consists of fine particles, whose sizes are below the critical ones and the magnetic moments vibrate with the frequency above the Larmor precession frequency, and the Mössbauer spectra are evidently contributed by these particles as the doublet lines. Increase of the substituting Mn ions in the $Co_{1-x}Mn_xFe_2O_4$ MNPs from $x = 0$ to $x = 1.0$ leads to increase in the line area of the paramagnetic doublet from 4 to 35%, which indicates decrease in the magnetic blocking temperature in the $MnFe_2O_4$ to the temperature slightly above the room temperature.

Taking into account that the paper [10] has established that the $Co_{1-x}Mn_xFe_2O_4$ MNPs at $x = 0.2$ ($Co_{0.2}Mn_{0.8}Fe_2O_4$) have a high value of the specific absorption rate (the most important parameter for the magnetic hyperthermia), it can be stated that the obtained results are important and useful for developing the MNPs, which are highly efficient for magnetic hyperthermia, by optimization of the composition of the solid solutions of the spinel ferrite nanoparticles.

Funding

I.M. Obaidat, V. Narayanaswamy, I.A. Al Omari, B. Issa express their gratitude to the University of Sharji and the Sharjah Research Academy for a grant No. 2101050262 for joint research.

Conflict of interest

The authors declare that they have no conflict of interest.

References

[1] Handbook of Nanomaterials for Industrial Applications. Author Chaudhery Mustansar Hussain. Elsevier Inc., Amsterdam, Netherlands (2018). 709 c.
[2] Z. Kai, J. Yanmin, X. Junjie, Y. Ziyu, G. Song, H. Yanglong. Acc. Chem. Res. **51**, 404 (2018).
[3] S. Dey, S.K. Dey, K. Bagani, S. Majumder, A. Roychowdhury, S. Banerjee, V.R. Reddy, D. Das, S. Kumar. Appl. Phys. Lett. **105**, 063110 (2014).
[4] B. Aslibeiki, P. Kameli, H. Salamati, G. Concas, M.S. Fernandez, A. Talone, G. Muscas, D. Peddis. Beilstein J. Nanotechnol. **10**, 856 (2019).
[5] A. Kaur, G.K. Bhargava. Mater. Today: Proc. **37**, 3082 (2021).
[6] Clinical Applications of Magnetic Nanoparticles / Ed. Nguyen T.K. Thanh. CRC Press. Taylor & Francis Group. (2018). P. 495.
[7] L. Peixoto, R. Magalhaes, D. Navas, S. Moraes, C. Redondo, R. Morales, J.P. Araujo, C.T. Sousa. Appl. Phys. Rev. **7**, 011310 (2020).
[8] M.M. Cruz, L.P. Ferreira, b, J. Ramos, S.G. Mendo, A.F. Alves, M. Godinho, M.D. Carvalho. J. Alloys Comp. **703**, 370 (2017).
[9] K. Islam, M. Haque, A. Kumar, A. Hoq, F. Hyder, S.M. Hoque. Nanomaterials **10**, 2297 (2020).
[10] V. Narayanaswamy, I.A. Al-Omari, A.S. Kamzin, B. Issa, H.O. Tekin, H. Khourshid, H. Kumar, A. Mallya, S. Sambasivam, I.M. Obaidat. Nanomaterials **11**, 1231 (2021).
[11] X. Wang, X. Kan, X. Liu, S. Feng, G. Zheng, Z. Cheng, W. Wang, Z. Chen, C. Liu. Mater. Today Commun. **25**, 101414 (2020).
[12] E. Umut. J. Hittite. Sci. Eng. **6**, 243 (2019).
[13] A.S. Kamzin, A.A. Valiullin, A. Bingolbali, N. Dogan. Physics of the Solid State **62**, 1091 (2020).
[14] S.P. Yadav, S.S. Shinde, Pramod Bhatt, S.S. Meena, K.Y. Rajpure. J. Alloys Comp. **646**, 550 (2015).
[15] K.M. Srinivasamurthy, V.J. Angadi, S.P. Kubrin, S. Matteppanavar, D.A. Sarychev, P. Mohan Kumar, H.W. Azale, B. Rudraswamy. Ceram. Int. **44**, 9194 (2018).
[16] A. Lassoued, M.S. Lassoued, F. Karolak, S. Garcia-Granda, B. Dkhil, S. Ammar, A. Gadri. J. Mater Sci: Mater. Electron. **28**, 18480 (2017).
[17] S.V. Bhandare, R. Kumar, A.V. Anupama, H.K. Choudhary, V.M. Jali, B. Sahoo. J. Magn. Magn. Mater. **433**, 29 (2017).
[18] A. Yang, C.N. Chinnasamy, J.M. Greneche, Y. Chen, S.D. Yoon, Z. Chen, K. Hsu, Z. Cai, K. Ziemer, C. Vittoria, V.G. Harris. Nanotechnology **20**, 185704 (2009).
[19] C. Pereira, A.M. Pereira, C. Fernandes, M. Rocha, R. Mendes, M.P. Fernández-García, A. Guedes, P.B. Tavares, J-M. Greneche, J.P. Araújo, C. Freire. Chem. Mater. **24**, 1496 (2012).
[20] F.G. da Silva, J. Depeyrot, A.F.C. Campos, R. Aquino, D. Fiorani, D. Peddis. J. Nanosci. Nanotechn. **19**, 4888 (2019).
[21] T. Dippong, E.A. Levei, O.C. Goga, D. Toloman, G. Borodi. J. Thermal Anal. Calorimetry **136**, 1587 (2019).
[22] A. Manohar, D.D. Geleta, C. Krishnamoorthi, J. Lee. Ceram. Int. **46**, 28035 (2020).
[23] S. Gandhi, S. Issar, A.K. Mahapatro, I. Roy. J. Mol. Liquids **310**, 113194 (2020).
[24] G. Lavorato, M. Alzamora, C. Contreras, G. Burlandy, F.J. Litterst, E. Baggio-Saitovitch. Part. Syst. Charact. 1900061 (2019).
[25] C.R. Alves, R. Aquino, J. Depeyrot, F.A. Tourinho, E. Dubois, R. Perzynski. J. Mater. Sci. **42**, 2297 (2007).
[26] R.M. Tripathi, S. Mahapatra, R. Raghunath, V.N. Sastry, T.M. Krishnamoorthy. Sci. Total. Environ. **250**, 43 (2000).
[27] J.Z. Msomi, H.M.I. Abdallah, T. Moyo, A. Lancok. J. Magn. Magn. Mater. **323**, 471 (2011).
[28] E. RanjithKumar, A.S. Kamzin, K. Janani. J. Magn. Magn. Mater. **417**, 122 (2016).
[29] M.I.A.A. Maksoud, G.S. El-Sayyad, M.A. Elkodous, A.S. Awed. J. Mater. Sci.: Mater. Electron. **31**, 9726 (2020).
[30] E. Zachanowicz, A. Zięcina, P.A. Mikołajczyk, K. Rogacki, M. Małecka, K. Marycz, M. Marędziak, B. Poźniak, M. Nowakowska, M. Tikhomirov, J. Miller, R.J. Wiglusz, R. Pązik. Eur. J. Inorg. Chem. **34**, 5315 (2016).
[31] C.J. Prabagar, S. Anand, M. Asisi Janifer, S. Pauline. Mater. Today: Proc. **47**, 2013 (2021).
[32] W.S. Sarifuddin, U.B. Purnama. J. Phys. Theor. App. **4**, 36 (2020).
[33] M.S. Angotzi, V. Mameli, D. Zákutná, D. Kubániová, C. Cara, C. Cannas. J. Phys. Chem. C **125**, 20626 (2021).
[34] P. Vlazan, I. Miron, P. Sfirloaga. Ceram. Int. **41**, 3760 (2015).
[35] S.F. Nasrin, U.Z. Chodhury, S.M. Hoque. J. Magn. Magn. Mater. **479**, 126 (2019).
[36] R. Jabbar, S.H. Sabeeh, A.M. Hameed. J. Magn. Magn. Mater. **494**, 165726 (2020).
[37] I.M. Obaidat, V. Narayanaswamy, S. Alaabed, S. Sambasivam, C.V.V.M. Gopi. Princip. Magn. Hyperthermia. Magnetochemistry **5**, 67 (2019).
[38] S.P. Yadev, S.S. Shinde, A.A. Kadam, K.Y. Rajpure. J. Semiconductor. **34**, (2013).
[39] A. Maksoud, G. El-Sayyad, A. Ashour, A. El-Batal, M. Elsayed. J. Microbial Phatogenesys **127**, 144 (2019).
[40] W.S. Sarifuddin, U.B. Purnama. AIP Conf. Proc. **2202**, 020024-1 (2019).
[41] N.N. Greenwood, T.G. Gibb, Mössbauer Spectroscopy. Chapman and Hall Ltd., London (1971).
[42] V. Kuncser, O. Crisan, G. Schinteie, F. Tolea, P. Palade, M. Valeanu, G. Filoti. Modern Trends in Nanoscience. Editura Academiei Romane, Bucharest (2013). V. 197.
[43] A.S. Kamzin, I.M. Obaidat, A.A. Valiullin, V.G. Semenov, I.A. Al-Omari. Physics of the Solid State **62**, 1919 (2020).
[44] A.S. Kamzin, I.M. Obaidat, V.S. Kozlov, E.V. Voronina, V. Narayanaswamy, I.A. Al-Omari. Physics of the Solid State **63**, 807 (2021).
[45] A.S. Kamzin, I.M. Obaidat, V.S. Kozlov, E.V. Voronina, V. Narayanaswamy, I.A. Al-Omari. Physics of the Solid State **63**, 900 (2021).
[46] V.G. Semenov, V.V. Panchuk. Mössbauer Spectra Processing Software MossFit. Private message.
[47] C.V. Ramana, Y.D. Kolekar, K.K. Bharathi, B. Sinha, K. Ghosh. J. Appl. Phys. **114**, 183907 (2013).
[48] H.S. Mund, B.L. Ahuja. Mater. Res. Bull. **85**, 228 (2017).
[49] R.M. Freire, T.S. Ribeiro, I.F. Vasconcelos, J.C. Denardin, E.B. Barros, Giuseppe Mele, L. Carbone, S.E. Mazzetto, P.B.A. Fechine. J. Nanopart. Res. **15**, 1616 (2013).
[50] H. Mansour, H. Letifi, R. Bargougui, S. De Almeida-Didry, B. Negulescu, C. Autret, A. Gadri, S. Ammar. Appl. Phys. A **123**, 787 (2017).
[51] W. Wang, Zui Ding,1 Xiruo Zhao, Sizhu Wu, Feng Li, Ming Yue, J. Ping Liu. J. Appl. Phys. **117**, 17A328 (2015); https://doi.org/10.1063/1.4917463

[52] G.R. Patta, V. Chitti Babu, V. Ravi Kumar, N. Veeraiah. J. Sol-Gel Sci. Technol. **100**, 310 (2021).
[53] M. De Marco, X.W. Wang, R.L. Snyder, J. Simmens, S. Bayya, M. White, M.J. Naughton. J. Appl. Phys. **73**, 6287 (1993).
[54] M. Atif, R. Sato Turtelli, R. Grössinger, M. Siddique, M. Nadeem. Ceram. Int. **40**, 471 (2014).
[55] G. Datt, C. Kotabage, S. Datar, A.C. Abhyankar. Phys. Chem. Chem. Phys., **20**, 26431 (2018).
[56] M.F. Etier, V.V. Shvartsman, F. Stromberg, J. Landers, H.W. Doru, C. Lupascu. Mater. Res. Soc. Symp. Proc. **1398**, 1 (2012). DOI: 10.1557/opl.2012.699
[57] T. Tatarchuk, M. Liaskovska, V. Kotsyubynsky, M. Bououdina. Mol. Cryst. Liquid Cryst. **672**, 54 (2018).
[58] H.M.I. Abdallah, T. Moyo, J.Z. Msomi. J. Phys: Conf Ser. **217**, 012141 (2010). DOI: 10.1088/1742-6596/217/1/012141
[59] S.B. Singh, Ch. Srinivas, B.V. Tirupanyam, C.L. Prajapat, M.R. Singh, S.S. Meena, Pramod Bhatt, S.M. Yusuf, D.L. Sastry. Ceram. Int. **42**, 19188 (2016). http://dx.doi.org/10.1016/j.ceramint.2016.09.081
[60] G.A. Sawatzky, F. Van Der Woude, A.H. Morrish. J. Appl. Phys. **39**, 1204 (1968).
[61] G.A. Sawatzky, F. Van Der Woude, A.H. Morrish. Phys. Rev. **187**, 747 (1969).
[62] S. Mørup, M.F. Hansen, C. Frandsen. Comprehensive Nanosci. Technology **1**, 437 (2011).
[63] S. Mørup, E. Brok, C. Frandsen. J. Nanomaterials ID 720629 (2013).
[64] W. Baaziz, B.P. Pichon, S. Fleutot, Y. Liu, C. Lefevre, J.-M. Greneche, M. Toumi, T. Mhiri, S. Begin-Colin. J. Phys. Chem. C **118**, 3795 (2014).
[65] I. Sharifi, H. Shokrollahi. J. Magn. Magn. Mater. **324**, 2397 (2012).
[66] Y. Shi, J. Ding, H. Yin. J. Alloys Comp. **308**, 290 (2000).
[67] S. Ayyappan, J. Philip, B. Raj. J. Phys. Chem. C **113**, 590 (2009).
[68] Y. Kim, D. Kim, C.S. Lee. Physica B **337**, 42, (2003).
[69] M. Liu, M. Lu, L. Wang, S. Xu, J. Zhao, H. Li. J. Mater. Sci. **51**, 5487 (2016).
[70] W.J. Schuele, S. Shtrikman, D. Treves. J. Appl. Phys. **36**, (Pt. 2), 1010 (1965).
[71] B.D. Kovacheva, T. Ruskov, P. Krystev, S. Asenov, N. Tanev, I. Mönch, R. Koseva, U. Wolff, T. Gemming, M. Markova-Velichkova, D. Nihtianova, K.-F. Arndt. Bulgarian Chem. Comm. **44**. Proc. of the 3-rd National Crystallographic Symposium (2012). P. 90–97.